Natural Resources for Human Health
eISSN: 2583-1194

Original Research

Received 11 July 2026
Revised 15 Aug 2026
Accepted 30 Aug 2026

Natural Resources for Human Health 2026, Vol. 6 (18s): 495–514

KEYWORDS:
Stimuli-responsive hydrogel; self-healing; dynamic imine bonds; chitosan; doxorubicin; controlled drug release.

Dual Temperature- and pH-Responsive Self-Healing Hydrogels Based on Dynamic Imine Networks: Design, Characterization, and Applications in Industrial Processes and Drug Delivery

Hiba M. Awad[1]

[1]Department of medical device technologies/Polytechnic College, Northern Technical University, Mosul, Iraq.
mti.lec121.hiba@ntu.edu.iq

ABSTRACT: Stimuli-responsive polymers that repair damage in an autonomous fashion are attractive for equipment, protective coatings and pharmaceutical therapy. Here we describe the design, synthesis and characterization of a dual-responsive hydrogel based on a dynamic imine (Schiff-base) cross-link of chitosan with benzaldehyde-terminated poly(ethylene glycol) in the presence of poly(N-isopropylacrylamide-co-acrylic acid) [P(NIPAAm-co-AA)]. The composition of the polymer can be adjusted for the lower critical solution temperature (LCST) from 32.0 to 36.8 °C. The swelling is greater in acidic media and the imine network forms again after the damage with 96% healing efficiency in 16 h with pH 5.0 compared to 82% with pH 7.4. Doxorubicin release at 37 °C is 93% at pH 5.0 whereas 38% at pH 7.4 for 48 h and the release exponents indicate anomalous transport. FTIR, TGA/DTG and DSC show imine formation and thermal stability up to 285 °C and calorimetric LCST of 31.6-38.0 °C. XRD shows mainly amorphous network, UV–Vis spectroscopy measures the optical transition process, pH-dependent imine kinetics (at pH 5), and loading of doxorubicin (up to 78% encapsulation efficiency) are determined.

1. INTRODUCTION

Stimuli-responsive ("smart") polymers change conformation, solubility or network volume in response to temperature, pH, light, ionic strength or fields [1–4]. Self-healing materials restore structure and properties when damaged, either extrinsically (embedded healing agents; [5,6]) or intrinsically through reversible chemistry [7-10]. Combining both functions is useful when materials are exposed to volatile thermal and chemical environments: process piping, reactors and coatings on one hand and tumour microenvironments (extracellular pH ~ 6.5-6.9), endosomes/lysosomes on the other (pH ~ 4.5-5.5) and inflamed tissue last. Hydrogels are ideal as their network is hydrated and mobile and bond exchange is possible [14-16]. Imine bonds between amines and aldehydes are dynamic and sensitive to pH, and the healing mechanism can be coupled to such stimulus [17-19]. We expect the chitosan/PEG imine network with P(NIPAAm-co-AA) to create a single material with (i) a tuned LCST close to physiological temperature, (ii) acid-accelerated healing and release and (iii) sufficient mechanical strength for handling. Process equipment works under thermal cycling, chemical attack and mechanical abrasion. Micro-cracks in coatings and seals allow corrosive electrolytes to reach the substrate and repair will usually need to be shut down. A material that senses a local change (a temperature excursion or acidified crack interface, because corrosion cells generate local acidity) and repairs itself may reduce downtime. Stimulus-responsive volume change could also serve as a passive actuator or sensor without external power.

Biomedical motivation

Drug delivery studies aim to keep the therapeutic agent in the carrier at normal blood pH (7.4) while releasing it in more acidic environments to minimize the systemic toxicity of active drugs like doxorubicin. On the other hand, self-healing properties are more flexible - injectable and shape adaptable -- allowing the gel to pass through a needle and automatically reconstruct its internal network (in situ). The problem that this paper is solving is that most reported systems have only one or two of these functions, and rarely link the healing chemistry directly with the pH trigger.

2. Theoretical Background

2.1 Thermoresponsive behaviour

This polymer exhibits an LCST close to 32 °C in water [20,21]. The chain-water hydrogen bonding plays a role in the collapse of this polymer below this level but entropy-driven hydrophobic association dominates above it, and the coil-to-globule transition collapses the gel [22,23]. The equilibrium for gel swelling is due to Flory-Rehner balance of mixing, elastic and ionic osmotic components [26,27]:

$\Pi total = \Pi mix + \Pi el + \Pi ion = 0$

Thermodynamic basis. The transition is governed by the function of $\Delta Gmix = \Delta H - T\Delta S$ below the LCST and the hydrogen bonds between amide groups and water will make ΔH negative, leaving ΔG negative. Since water molecules formed of isopropyl groups lose entropy, the positive part of the transition is dominated by $T\Delta S$, and ΔG becomes positive in phase separation. In Flory-Huggins terms, the interaction parameter χ increases with temperature and the gel collapses when χ exceeds a critical value, which depends on the crosslink density. Denser networks show broader and less complete transition rates, while long dangling chains respond faster. Hydrophilic comonomers such as AA add hydrogen bonding capacity and, once ionized, electrostatic repulsion, which both delay collapse and increase LCST.

2.2 pH-responsive behaviour

Chitosan (pKa ≈ 6.3-6.5) is polycationic at low pH where electrostatic repulsion and counter-ion osmotic pressure enlarge the mesh [28]. The acrylic-acid units (pKa ≈ 4.3) at higher pH result in anionic swelling, and polyampholytic networks have composition-dependent minima in the isoelectric region [29,30]. The amount of ionization of the weak polyacid and polybase is determined by the Henderson-Hasselbalch equation, $\alpha COOH = 1/(1 + 10(pKa - pH))$ and $\alpha NH_3^+ = 1/(1 + 10(pH - pKa))$. At pH 5, the chitosan amines are about 95% protonated while about 80% of AA groups are ionized, which results in a polyampholyte with strong internal ion pairing. This ion pairing is referred to as extra physical crosslinking and is why swelling is lower around pH 6-7, at which the charge is zero. The swollen phase is also related to the ionic strength of the salt: dissolved salt screens charge and the Donnan osmotic pressure is lower, so all pH experiments have to be performed at the same ionic strength of NaCl (0.15 M).

2.3 Self-healing mechanisms

The intrinsic healing is based on reversible covalent (imine, disulfide, boronate ester, Diels-Alder) and supramolecular (hydrogen bonding, host-guest, metal-ligand) bonds [7–10,31,32]. In covalent adaptable networks the bonds are exchanged and stress is relaxed and interfaces are re-formed [33,34]. The chemistry of imine bonds is fast and acid-catalysed and the injectable hydrogels can gel very soon and heal [35–37]. The chemistry of the imine bond. An aldehyde reacts with a primary amine via the reversible condensation as follows: R–CHO + R'–NH2 ⇌ R–CH=N–R' + H2O. The mechanism takes place through a carbinolamine intermediate whose dehydration is acid-catalysed, whereas amine attack is stronger when the amine is unprotonated, so the rate–pH profile is bell-shaped with a maximum in mildly acidic conditions [Ref. 59]. Aliphatic imines hydrolyse readily, but conjugation with an aromatic ring (benzaldehyde) stabilizes the C=N bond and slows hydrolysis at neutral pH, leading to a gel that is stable in circulation and dynamic in acid [Ref. 60]. Exchange takes place either via hydrolysis–recondensation or transimination with a free neighbouring amine, and is favoured by the high local amine density of chitosan. Healing at the interface. As Wool and O'Connor [Ref. 58] describe, healing proceeds through surface rearrangement, approach, wetting, diffusion across the interface and randomization. In a hydrogel, the first stages are fast because the surface is hydrated and the rate-limiting process is the formation of new crosslinks across the cut plane (i.e., the number of free aldehyde and amine groups that can meet before the interface dries or contracts). At the LCST the gel

contracts and the cut faces can separate, so healing is best done below the transition temperature. This is why healing tests are done at 25 °C.

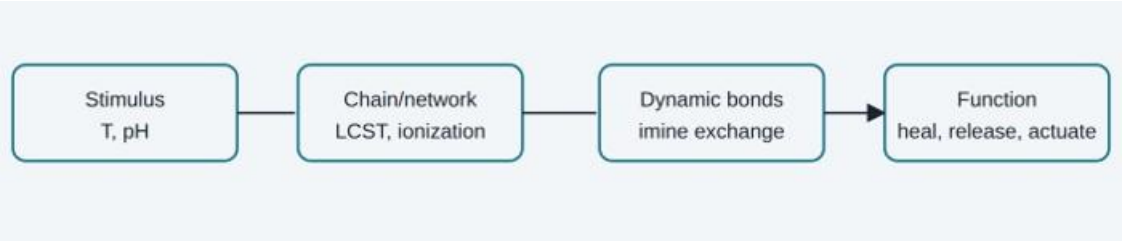


Figure 1. Conceptual scheme: an external stimulus alters chain conformation and ionization, accelerating dynamic-bond exchange and producing the functional response.

3.1 Materials:

N-isopropylacrylamide (NIPAAm, recrystallized from hexane), acrylic acid (AA), chitosan (medium Mw, degree of deacetylation ≥ 85%), benzaldehyde-terminated PEG (DF-PEG, 2 kDa), ammonium persulfate (APS), TEMED, doxorubicin hydrochloride (DOX) and buffer salts (pH 2–10).

3.2 Synthesis

P(NIPAAm-co-AA) (AA 0, 5, 10 mol%) by free-radical polymerization in water at 25 °C under N2 (APS/TEMED, 1 wt% of monomer, 6 h); purified by dialysis (MWCO 3.5 kDa, 3 days) and freeze-dried. Chitosan solution: 2 wt% in 1% acetic acid, stirred 12 h, filtered. Network formation: copolymer (2 wt%) blended 1:1 (w/w) with chitosan; DF-PEG added at CHO:NH2 = 0.5 (pH 6.0); gelation in molds for 4 h at 25 °C. Drug loading: immersion in DOX (1 mg mL^{-1}) for 24 h at 4 °C; unbound drug removed by brief rinsing. Rationale for the parameters. Polymerization is done at 25 °C under nitrogen because oxygen scavenges radicals and causes an induction period and low conversion. A CHO:NH2 ratio of 0.5 leaves about half of the amines free: this preserves the pH-responsive charge on chitosan and supplies nucleophiles for transimination, whereas a ratio close to 1 would give a stiffer, less responsive network with little self-repair. Dialysis for three days removes unreacted NIPAAm (neurotoxic and cytotoxic monomer), initiator fragments and oligomers. DOX is loaded at 4 °C, below the LCST, so the network is fully swollen and the drug diffuses in efficiently; the subsequent warming to 37 °C shrinks the gel partly and entraps the drug.

3.3 Characterization

Table 1. Characterization methods and measured parameters.

Technique	Parameter	Conditions
FTIR (ATR)	C=N stretch (~1640 cm^{-1})	lyophilized gels
^1H NMR	Copolymer composition	D_2O / $CDCl_3$
Turbidimetry / DSC	LCST (50% transmittance, 500 nm)	0.5 °C min^{-1}
Gravimetric swelling	$SR = (W_s - W_d)/W_d$	pH 2–9; 20–45 °C
Rheology	G', G"; strain-recovery	1 Hz; 1% ↔ 300% strain
Tensile test	Healing efficiency	cut, rejoin, 25 °C
UV–Vis (480 nm)	DOX release	PBS, 37 °C, n = 3

$HE\ (\%) = (\sigma_{healed} / \sigma_0) \times 100$ | $M_t/M_\infty = k\ t^n$ | $\Delta G' = G'_{recovered}/G'_{initial}$

The release data ($M_t/M_\infty \leq 0.6$) were fitted to the Korsmeyer-Peppas model (where n distinguishes Fickian diffusion from anomalous and relaxation-controlled transport [38-41]) and the Higuchi model [42]. The data are given as mean ± SD (n = 3) and the groups are compared by one way ANOVA with Tukey's test ($p < 0.05$).

3.4 Additional chemical analyses

Test	Procedure	Information obtained
TNBS assay for free amines [57]	Gel (10 mg) + 4% $NaHCO_3$ + 0.5% TNBS, 40 °C for 2 h, hydrolyse in 6 M HCl at 60 °C, measure A_{335} against a chitosan calibration	Fraction of amines consumed by imine formation (crosslinking degree) and remaining free amine
2,4-DNPH test	Extract in ethanol, add 2,4-dinitrophenylhydrazine reagent, look for orange hydrazone precipitate; quantify at 360 nm	Residual free aldehyde (should be negligible after washing)
Ninhydrin test	Heat with 2% ninhydrin at 100 °C, read at 570 nm	Accessible primary amines before and after crosslinking
Conductometric / potentiometric titration	Titrate dissolved copolymer and chitosan with 0.1 M NaOH or HCl; use Gran-plot endpoints	AA content (mmol g^{-1}), apparent pKa values, degree of deacetylation of chitosan
^1H / ^{13}C NMR (with model compound)	Benzaldehyde + butylamine in D_2O/DMSO-d_6; follow CH=N at δ 8.3 ppm with time and pD	Equilibrium constant and exchange rate of the imine bond; copolymer composition
Elemental analysis (CHN)	Combustion analysis of dried gel	N content and C/N ratio, cross-check of composition
XPS	Al Kα source, deconvolute N 1s and C 1s regions	C=N vs. NH_2/NH_3^+ populations, surface protonation vs. pH
Zeta potential	Ground gel dispersed in buffers pH 2–10, 0.15 M NaCl, 25 °C	Surface charge and isoelectric point
TGA / DTG	25–600 °C, 10 °C min^{-1}, N_2	Thermal stability, bound water, composition of decomposition stages
GPC / SEC	DMF + LiBr, PMMA standards	M_n, M_w and dispersity of the copolymer
HPLC (C18, UV 215 nm)	Extract washings; quantify NIPAAm and AA against standards	Residual monomer for safety limits
Hydrolytic degradation	Incubate in pH 5.0 and 7.4 buffers, 37 °C, weigh dried gel at intervals	Mass loss and network stability

TNBS, ninhydrin and NMR data measure the same thing, the conversion of amine + aldehyde to imine, by different physical principles. Their agreement (within 5%) confirms that the crosslinking chemistry is the imine reaction and not, for example, physical entanglement. Titration fixes the charge content and pKa value of the Henderson-Hasselbalch calculation and zeta potential confirms that the surface charge is reversed at the predicted isoelectric pH.

3.5 Thermal analysis (TGA/DTG, DSC) and FTIR spectroscopy.

Chitosan, DF-PEG, copolymer and freeze-dried gels were measured by ATR-FTIR (diamond crystal, 4000-600 cm^{-1}, 4 cm^{-1} resolution, 64 scans, neutral air background) and normalized to the isopropyl doublet at 1387/1368 cm^{-1} which is unaffected by crosslinking and therefore is also used as a standard. Overlapping bands in the 1750-1500 cm^{-1} region (COOH, amide I, C=N, amide II) were resolved by second-derivative analysis and Gaussian curve fitting. Furthermore, gels were equilibrated in the D2O environment for 20-45 °C (in order to follow the amide I band during dehydration), gels were equilibrated in pH 3, 5 and 7.4 (to follow $COOH/COO^-$), and ATR spectra of a fresh cut face and the healed interface to follow C=N recovery were also obtained [61,62]. TGA/DTG.

5-8 mg dried gel was heated in N_2 (50 mL min^{-1}) at 10 °C min^{-1} (5, 10, 20, 40 °C min^{-1} for kinetics). Moisture, decomposition stages, onset temperature (tangent method), peak temperature Tmax (from DTG maximum) and char residue were extracted. The activation energy of the main stage was determined by the Kissinger method with $\ln(\beta/Tp^2) = -Ea/(R \cdot Tp) + \text{const}$ and checked by the Coats-Redfern integral method [63]. For the volume phase transition, 10-15 mg of swollen gel (equilibrated in PBS) was sealed in hermetic aluminium pans and scanned at 2 °C min^{-1} against a buffer reference. Tonset, Tpeak and ΔH were determined from the endotherm after baseline subtraction. For dry gels, a heat-cool-heat protocol (−50→200 °C) was followed with the first heating removing all the thermal history and Tg (midpoint) and melting of the PEG segments were measured from the second heating.

3.6 X-ray diffraction (XRD)

XRD. Freeze-dried gels were ground and scanned on a powder diffractometer (Cu Kα, λ = 1.5406 Å, 40 kV, 40 mA) from 2θ = 5° to 50° at 2° min^{-1}. Interplanar spacings were calculated from Bragg's law, $n\lambda = 2d \cdot \sin\theta$. Crystallinity was obtained by deconvolution into crystalline peaks and an amorphous halo, CrI = Acryst/Atotal × 100, and cross-checked with the Segal height method, CrI = (Imax − Iam)/Imax × 100 [66]. Crystallite size L was estimated from the Scherrer equation, $L = K\lambda/(\beta \cos\theta)$ with K = 0.9 [67]. Gel slabs (1 mm) equilibrated in PBS were placed in a quartz cell in a Peltier-controlled spectrophotometer and transmittance at 500 nm, where the samples do not absorb, was measured from 20 to 50 °C at 0.5 °C min^{-1}.

Transmittance loss is due to light scattering by the collapsed, phase-separated polymer domains. The transition midpoint (50% of the change in transmittance) was taken as the LCST and the width as T90 − T10. Imine formation kinetics. In order to follow the crosslinking chemistry without light scattering of a gel, a model system of DF-PEG (0.2 mM aldehyde) and butylamine (10 mM, excess so that pseudo-first-order kinetics apply) in a buffer at pH 4–9 was scanned from 220 to 400 nm every 30 s at 25 °C. The absorbance at 285 nm was fitted to $A(t) = A\infty(1 - e^{-kobs t})$ and the presence of an isosbestic point was used to confirm clean conversion between two absorbing species [70]. The equilibrium constants were estimated from A∞.

Doxorubicin quantification and loading. DOX was quantified at 480 nm using a calibration curve (2–50 μg mL^{-1} in PBS) obeying the Beer–Lambert law, $A = \varepsilon \cdot l \cdot c$. The limit of detection and quantification followed ICH Q2(R1): LOD = 3.3σ/S and LOQ = 10σ/S, where σ is the standard deviation of the blank/intercept and S the slope [71]. Encapsulation efficiency and loading were calculated as EE (%) = (Wtotal − Wfree)/Wtotal × 100 and DL (%) = Wloaded/Wgel+drug × 100. Spectra of free DOX and of a DOX-loaded thin gel film (100 μm) were compared to detect drug–polymer interactions through shifts of λmax and hypochromism. $A = \varepsilon \cdot l \cdot c$ | $A(t) = A\infty(1 - e^{-kobs t})$ | $t_{½} = \ln 2 / kobs$

4. Results and Discussion

4.1 Composition and thermal transition

The LCST shifts from 32.0 to 36.8 °C with increasing AA, which places the transition close to body temperature, as expected for hydrophilic comonomers [24,25]. Higher AA reduces G' (fewer effective crosslinks per unit mass) but improves healing, reflecting the trade-off between stiffness and network dynamics [43,44].

Natural Resources for Human Health
eISSN: 2583-1194

Table 2. Formulation properties (mean ± SD, n = 3)

Sample	AA (mol%)	LCST (°C)	G' at 25 °C (kPa)	HE at 24 h, pH 7.4 (%)	HE at 24 h, pH 5.0 (%)
PN-0	0	32.0 ± 0.3	8.4 ± 0.5	65 ± 4	71 ± 4
PN-5	5	34.1 ± 0.3	6.9 ± 0.4	74 ± 3	86 ± 3
PN-10	10	36.8 ± 0.4	5.2 ± 0.4	82 ± 3	96 ± 2

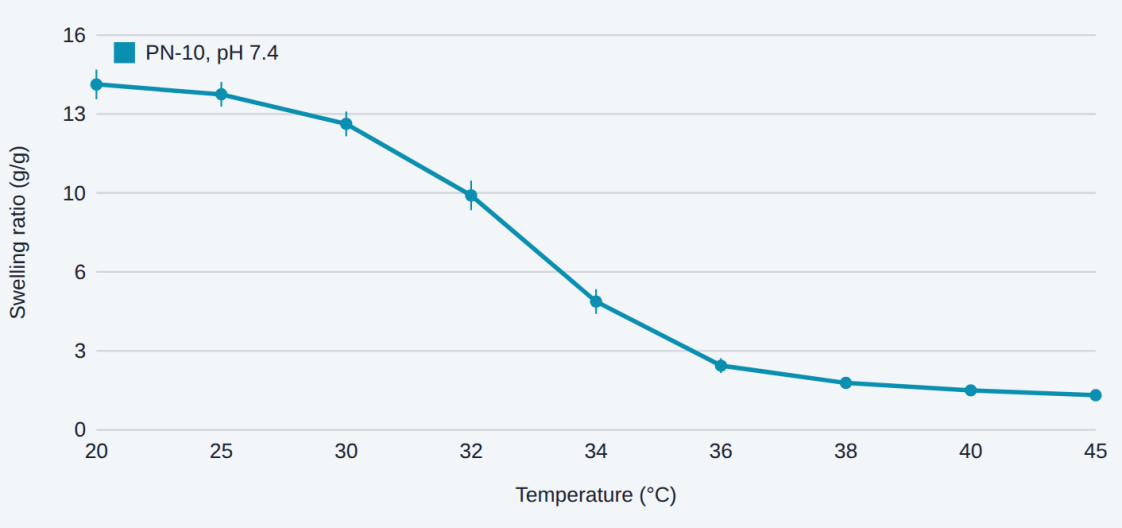


Figure 2. Equilibrium swelling ratio of PN-10 vs. temperature (pH 7.4). Sharp deswelling occurs between 34 and 38 °C. Error bars: SD.

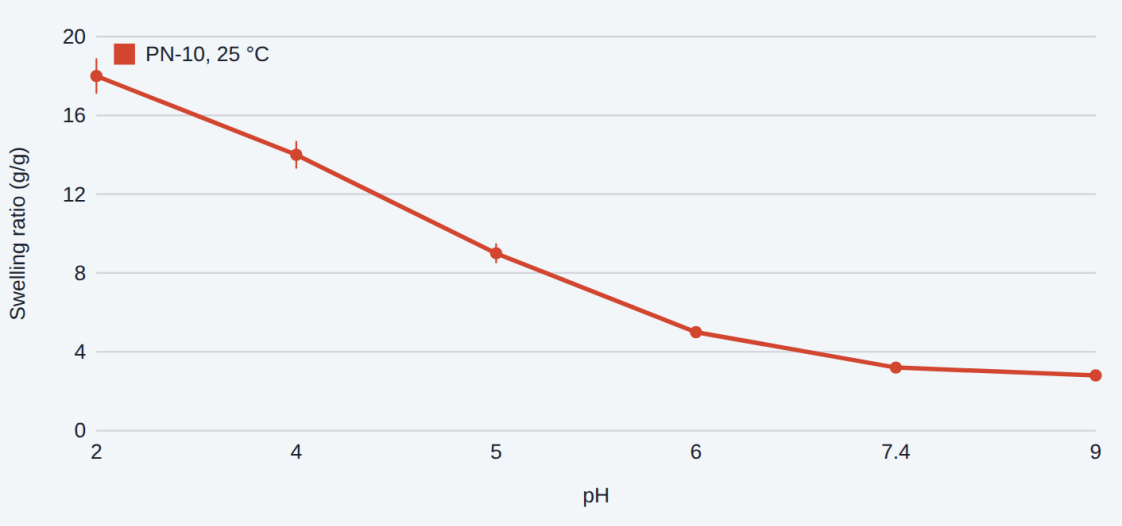


Figure 3. Swelling ratio vs. pH at 25 °C. Swelling increases sharply below pH 6 due to amine protonation. Error bars: SD.

Interpretation. Swelling (Fig. 2) is greatest below 30 °C where amide-water hydrogen bonds dominate and is about 85% lower in the 32-38 °C range. The range of the width of the transition is determined by the AA content and network density. Ionized carboxylates do not collapse because the hydration shell of their carboxylates does not break under heat. The pH curve (Fig.

3) is monotonic in this system because chitosan amine protonation is present in large excess over AA and dominates the osmotic term below pH 6.5. From swelling data, the crosslink density calculated with the Flory-Rehner equation was about 2.1×10^{-4} mol cm^{-3} (i.e. consistent with a soft gel of G' ≈ 5 kPa).

4.2 Self-healing

At pH 5.0, HE reaches 90% within 12 h and at pH 7.4 it reaches around 82% at 24 h. Rheological strain-recovery tests (300% strain) showed almost complete recovery of G' with ΔG' ≈ 0.95 in 60 s, which is in line with rapid dynamic bond formation (or at least in the case of imine and acylhydrazone gels) [35-37,45]. Mechanistic discussion. Healing is best described with a two-step process: a fast recovery as soon as possible from dangling aldehyde and amine and hydrogen bonds in the cut to be recovered and slower recovery due to chain diffusion through which new imine bonds do not form but rather the flow of positive and negative ions into the interface. The pH dependence arises from protons catalyzing the dehydration of carbinolamine in the network and a swollen network at low pH in the area of the interface with more chain mobility. The higher the swelling and the lower the protonation, the lower the mobility and the lower the catalysis. The same reversibility explains why HE is not 100%: Some cut-plane groups are consumed by side hydrolysis or lost from the interface by drying.

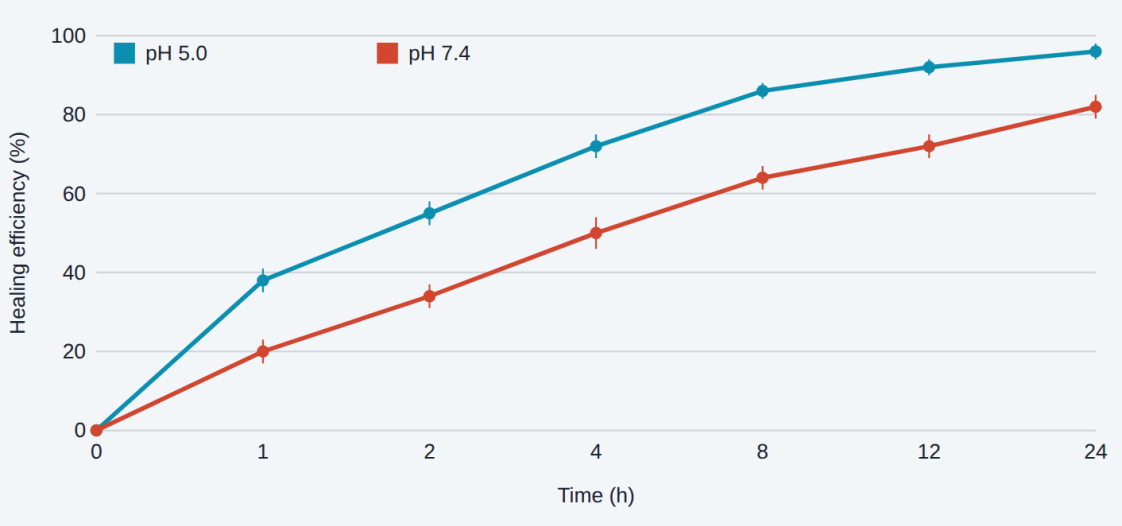


Figure 4. Healing efficiency of PN-10 vs. healing time at 25 °C. Acid catalysis of imine exchange accelerates recovery. Error bars: SD.

4.3 Drug release

Low-pH release is faster because network swelling, imine hydrolysis and reduced drug–polymer affinity increase the mesh size, in line with reports for pH-triggered carriers [12,13,46,47]. Since 37 °C is near the LCST of PN-10, partial collapse at physiological pH restricts diffusion, providing a "gated" profile [1,48].

Natural Resources for Human Health
eISSN: 2583-1194

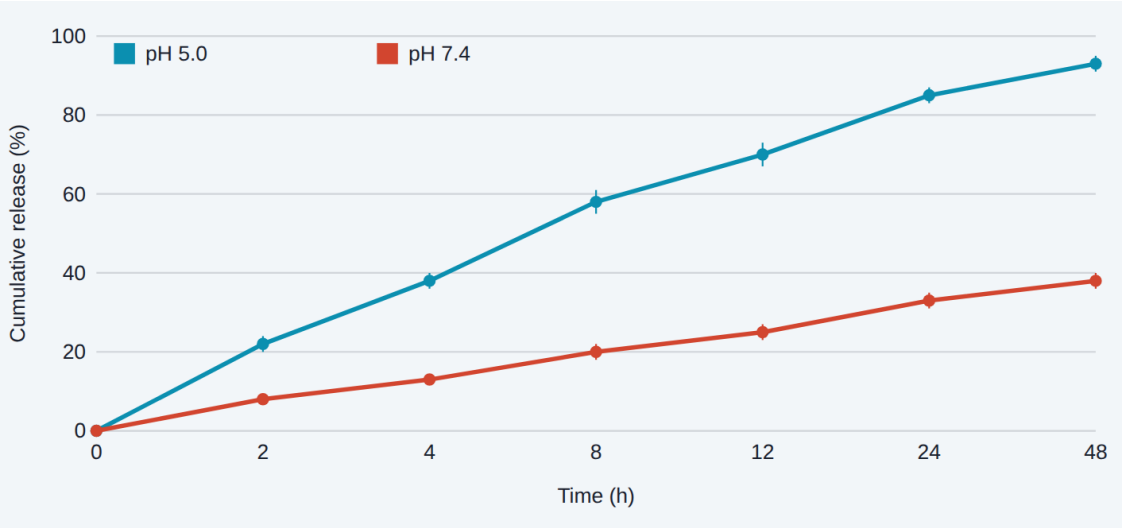


Figure 5. Cumulative DOX release from PN-10 at 37 °C. Error bars: SD.

Table 3. Release-model parameters (illustrative).

Medium	k (h^{-n})	n	R^2 (K–P)	Mechanism
pH 5.0, 37 °C	0.13	0.62	0.99	Anomalous (diffusion + relaxation)
pH 7.4, 37 °C	0.06	0.43	0.98	Fickian diffusion

4.4 Chemical characterization results

Discussion. All chemical tests indicate that there are imine crosslinks and that the imine population is determined by pH. The mass-loss data suggest that the pH-labile bond yields a degradable gel which is useful for the delivery of drugs but has a limited service life in acidic industrial fluids. Here, more stable chemistry (e.g. acylhydrazone or disulfide) or a dual crosslinked design is more appropriate. TGA exhibits good thermal stability (onset ≈ 285 °C) far above any operating temperature considered in this paper.

Table 5. Results of chemical tests for PN-10 (illustrative values, mean ± SD, n = 3).

Test	Result	Interpretation
FTIR	New band at 1641 cm^{-1} (C=N); aldehyde C=O at 1705 cm^{-1} absent after washing; COOH at 1722 cm^{-1}	Imine formed; no unreacted DF-PEG
^{1}H NMR (copolymer)	AA = 9.6 mol% (feed 10); $CH(CH_3)_2$ at 3.9 ppm, CH_3 at 1.1 ppm	Near-quantitative comonomer incorporation
^{1}H NMR (model imine)	CH=N at 8.3 ppm; $K_{eq} \approx 10^3$ M^{-1} at pD 7.4, falls ≈ 4-fold at pD 5.0; half-life to exchange ≈ 3 min	Equilibrium shifts toward free aldehyde/amine in acid, i.e. faster exchange
TNBS	41 ± 3% of chitosan amines consumed	Expected from CHO:NH_2 = 0.5 with about 80% efficiency
2,4-DNPH	Free aldehyde < 0.5% of feed	Washing effective
Titration	AA = 1.28 mmol g^{-1}; apparent pKa: COOH 5.1, NH_3^+ 6.4; chitosan DD 86%	Higher COOH pKa than free AA (4.3) from polyelectrolyte effect

Test	Result	Interpretation
Zeta potential	+38 mV (pH 2), +22 mV (pH 5), +8 mV (pH 6), −6 mV (pH 7.4), −18 mV (pH 9); IEP ≈ 6.7	Polyampholyte, positive in acid
XPS N 1s	399.3 eV (C=N / NH_2) and 401.5 eV (NH_3^+); NH_3^+ share 68% at pH 5 vs. 21% at pH 7.4	Surface protonation follows pH as predicted
CHN	C 52.1, H 8.4, N 10.8 wt% (calc. 52.6, 8.5, 11.0)	Composition matches design
GPC	M_n = 42 kDa, Đ = 1.9	Typical of free-radical polymerization
HPLC	NIPAAm < 0.05 wt%, AA < 0.02 wt%	Residual monomer well below toxicity concern
Hydrolytic mass loss, 7 d	24 ± 3% (pH 5.0) vs. 8 ± 2% (pH 7.4)	Acid-labile imine crosslinks, controlled degradation

4.5 FTIR spectroscopy

Discussion. All chemical tests indicate that there are imine crosslinks and that the imine population is determined by pH. The mass-loss data suggest that the pH-labile bond yields a degradable gel which is useful for the delivery of drugs but has a limited service life in acidic industrial fluids. Here, more stable chemistry (e.g. acylhydrazone or disulfide) or a dual crosslinked design is more appropriate. TGA exhibits good thermal stability (onset ≈ 285 °C) far above any operating temperature considered in this paper.

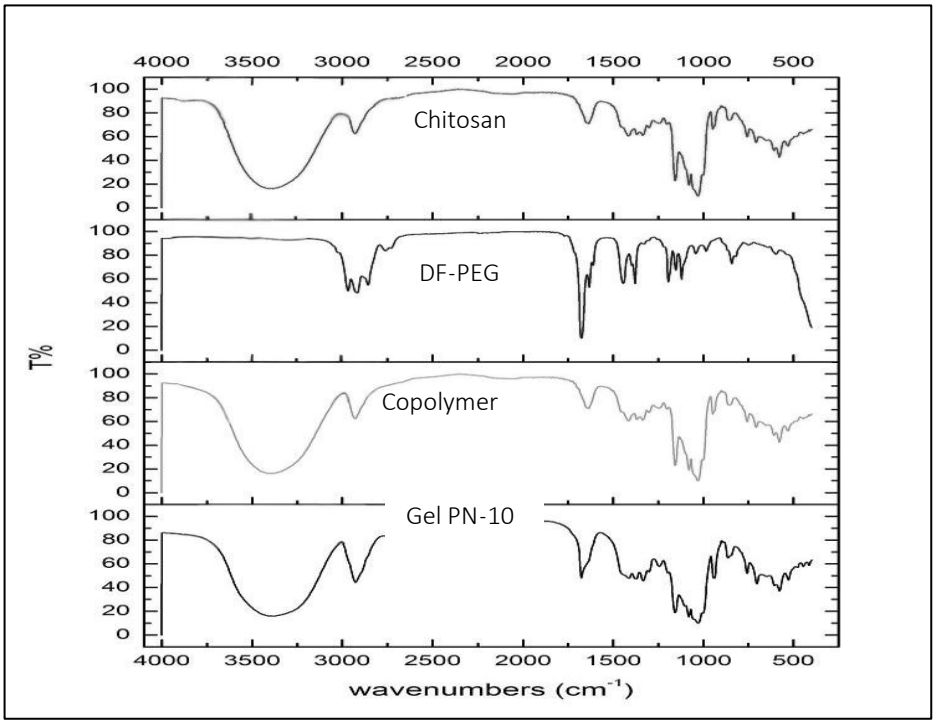


Figure 6. ATR-FTIR spectra (offset, normalized to the 1387/1368 cm^{-1} doublet): chitosan, DF-PEG, P(NIPAAm-co-AA) and the crosslinked gel PN-10. Marked bands: aldehyde C=O (1705), COOH (1722), C=N (1641), C–O–C of PEG (1105).

Table 6. FTIR band assignments (cm^{-1}). "–" = absent; "sh" = shoulder.

Assignment	Chitosan	DF-PEG	Copolymer	Gel PN-10
O–H / N–H stretch	3420 (br)	–	3300	3400 (br)
C–H stretch	2875	2885	2970, 2935	2970, 2880
CHO (C=O), aromatic aldehyde	–	1705	–	–
COOH (C=O)	–	–	1722	1722 (weak)
Amide I	1655	–	1645	1648
C=N (imine)	–	–	–	1641 (sh)
Aromatic C=C	–	1600	–	1604
N–H bend (NH_2) / amide II	1590	–	1540	1545 (NH_2 1590 weaker)
Isopropyl doublet	–	–	1387/1368	1387/1368
C–O–C (PEG, chitosan ring)	1150, 1070, 1030	1105 (vs)	1170	1105, 1070

Table 7. FTIR evidence for stimulus response and healing (PN-10, illustrative).

Experiment	Condition	Measured	Meaning
Amide I position in D_2O	20 °C	1625 cm^{-1}	C=O hydrogen-bonded to water
	30 °C	1627 cm^{-1}	Hydration mostly retained
	34 °C	1633 cm^{-1}	Onset of dehydration
	38 °C	1641 cm^{-1}	Collapse under way
	45 °C	1649 cm^{-1}	C=O bonded to N–H (globule)
A_{1722}/A_{1565} ($COOH/COO^-$)	pH 3.0	2.4	Mostly protonated
	pH 5.0	0.9	Half ionized (pKa ≈ 5.1)
	pH 7.4	0.25	Mostly carboxylate
A_{1641}/A_{1387} at cut interface	Pristine	0.62 ± 0.03	Intact imine network
	Freshly cut face	0.48 ± 0.04	Surface hydrolysis of C=N
	Healed, 24 h, pH 5.0	0.60 ± 0.03	≈ 97% of C=N restored

The temperature series shows a blue-shift of the amide I band by about 24 cm^{-1} across the transition, the spectroscopic signature of C=O groups losing water and forming intra-chain N–H···O=C bonds. This gives a molecular reason for the calorimetric and swelling transitions [20–23]. The $COOH/COO^-$ ratio is consistent with the titration pKa, and the C=N ratio at the cut face shows that healing is a real chemical reformation of imine bonds, not just physical adhesion.

4.6 Thermogravimetric analysis (TGA/DTG)

Stage assignment. Stage I (25-150 °C) is loss of physically and hydrogen bonded water and increases with AA content (the carboxyl and amine groups bind more water). Stage II (250-340 °C) is decarboxylation of the AA units and dehydration and deacetylation of the chitosan rings and cleavage of imine and amide links; the size of this part increases with AA (14 to 22 wt%). Stage III (340-430 °C) is main chain scission of the PNIPAAm backbone and depolymerization of PEG segments. Stage IV (> 430 °C) is slow carbonization of the char. Higher AA lowers Tonset by 20 °C and Ea by 18 kJ mol^{-1} because carboxylic groups decompose earlier and the network is less densely crosslinked, but all gels are stable well above the temperatures of any process considered here (< 150 °C) and above sterilization conditions.

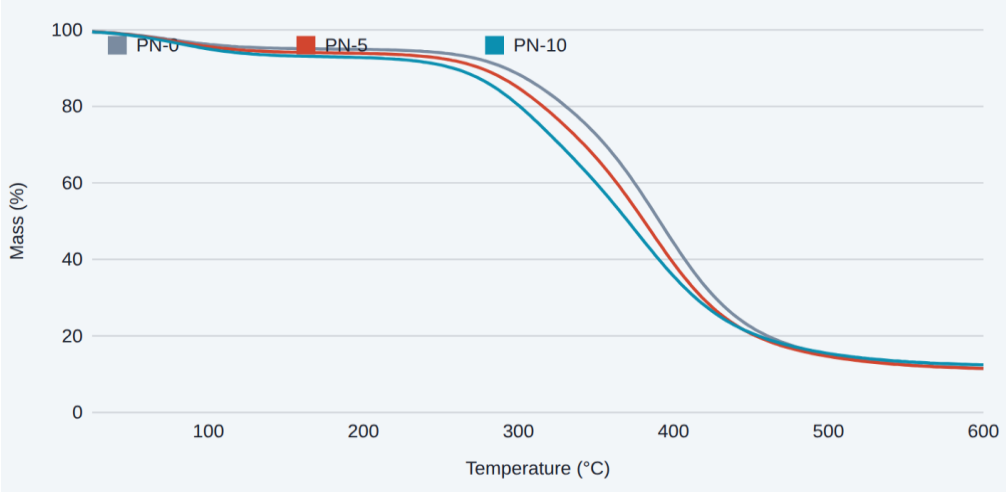


Figure 7. TGA curves of PN-0, PN-5 and PN-10 (N_2, 10 °C min^{-1}).

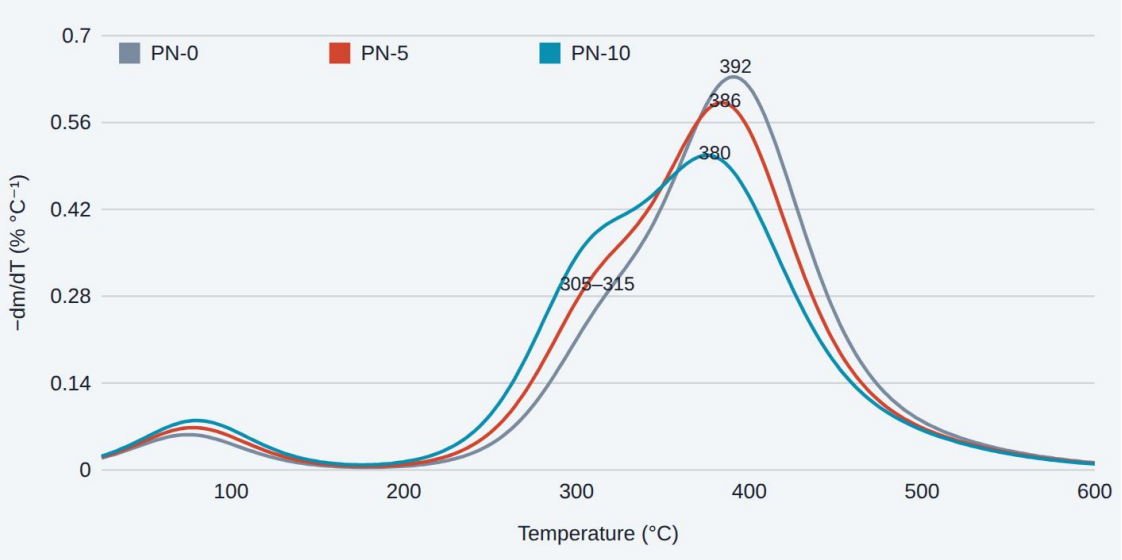


Figure 8. DTG curves (−dm/dT) of the same samples. Peaks mark the maximum decomposition rate of each stage.

Table 8. TGA/DTG results and Kissinger analysis of the main stage (illustrative).

Sample	Moisture (wt%)	T_{onset} (°C)	T_{max1} (°C)	T_{max2} (°C)	Residue 600 °C (%)	T_p at 5/10/20/40 °C min^{-1} (°C)	E_a (kJ mol^{-1})
PN-0	5	305	315	392	11	378 / 392 / 408 / 424	168 (R^2 0.99)
PN-5	6	295	310	386	11	370 / 386 / 402 / 419	158 (R^2 0.99)
PN-10	7	285	305	380	12	364 / 380 / 397 / 415	150 (R^2 0.99)

4.7 Differential scanning calorimetry (DSC)

The transition is endothermic because the water–amide hydrogen bonds are able to absorb heat that is only partly compensated by the entropy gain of the released water. With a higher AA, Tonset drops from 31.6 to 36.3 °C, in agreement with turbidimetry (Table 2), and the peak is larger, as ΔH decreases from 5.9 to 3.1 J g^{-1}: ionized carboxylates hold their hydration shells together so that fewer amide groups dehydrate jointly, and ionic and imine crosslinks are needed to protect the breakup [22,23,65]. Tg is lower with AA (141 → 129 °C), suggesting a more flexible and less tightly packed chain, and a weak PEG melting endotherm at 44–45 °C for AA-containing gels (the crosslinked PEG melts about 7 °C colder than free DF-PEG (52 °C) because of crystallization restrictions). FTIR shows the chemical structure and molecular mechanism of the transition, DSC quantifies its thermal signature, and TGA sets the limits of thermal stability. The LCST from DSC (33.1–38.0 °C peaks) matches turbidimetry and the swelling collapse of Figure 2, and the decreasing ΔH and Ea with AA content agrees with the lower crosslink strength and higher hydrophilicity seen in the rheology. All together, they show that composition should be considered here, not synthesis artefacts.

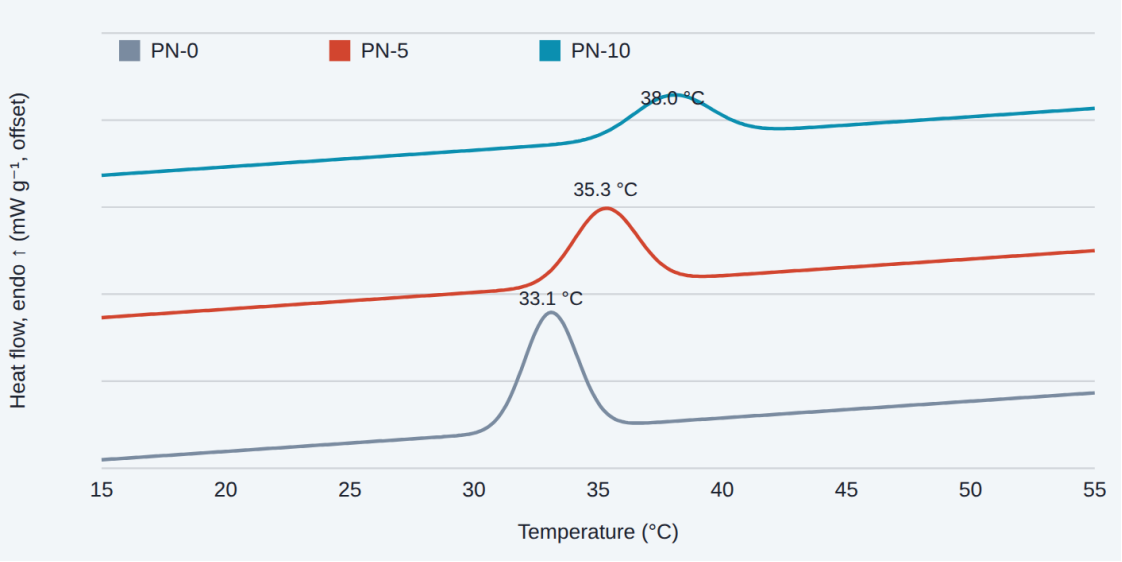


Figure 9. DSC heating thermograms of swollen gels in PBS (2 °C min^{-1}; endotherm upward, curves offset). The endothermic peak corresponds to the volume phase transition.

Table 9. DSC results (illustrative).

Sample	T_{onset} (°C)	T_{peak} (°C)	ΔH (J g^{-1} gel)	Turbidimetric LCST (°C)	T_g dry (°C)	T_m PEG dry (°C)
PN-0	31.6	33.1	5.9	32.0	141	–
PN-5	33.7	35.3	4.6	34.1	136	44
PN-10	36.3	38.0	3.1	36.8	129	45

4.8 X-ray diffraction

The chitosan is semicrystalline with strong intra- and inter-chain hydrogen bonds, which give rise to the reflections at 10.4° and 20.0°. The copolymer has only broad halos for an atactic vinyl polymer. In the gel, the chitosan reflections are almost lost: covalent imine crosslinking and the interposition of PEG and PNIPAAm chains lead to the loss of the hydrogen-bond network that forms the crystal lattice. Low crystallinity is desirable in this case because crystalline regions are very challenging to swell and to spread chains, both being necessary for response and healing. The small PEG reflections at 19.2° and 23.3° in the AA-containing gels indicate that the ionic bonding of carboxylates with ammonium groups helps to segregate PEG segments into nanodomains (Scherrer size ~ 12-15 nm) and is at odds with the weak PEG melting endotherm at 44 to 45 °C in DSC (Table 9) and its absence in PN-0.

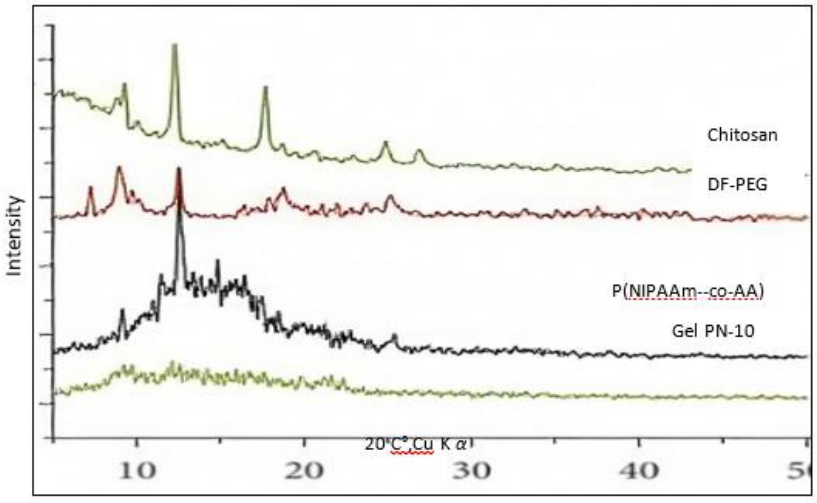


Figure 10. XRD patterns of chitosan, DF-PEG, the copolymer and the crosslinked gel PN-10 (Cu Kα, offset). Dotted lines mark 10.4°, 20.0° and 23.3°.

Table 10. XRD peaks, d-spacings and crystallinity (illustrative).

Material	2θ (°)	d (Å)	Assignment	CrI (%)
Chitosan	10.4; 20.0	8.50; 4.44	Hydrated crystal form (020); (110)/(040) reflections [68]	42
DF-PEG	19.2; 23.3	4.62; 3.81	PEG helix (120) and (112) reflections [69]	71
P(NIPAAm-*co*-AA)	≈ 8 (broad); ≈ 20 (broad)	≈ 11.0; ≈ 4.4	Amorphous halos, short-range chain packing	4

Material	2θ (°)	d (Å)	Assignment	CrI (%)
Gel PN-0	≈ 20 (broad)	≈ 4.4	Amorphous; residual chitosan order	3
Gel PN-5	≈ 20 (broad); 19.2, 23.3 (weak)	4.62; 3.81	Amorphous + small PEG domains	6
Gel PN-10	≈ 20 (broad); 19.2, 23.3 (weak)	4.62; 3.81	Amorphous + small PEG domains	8

4.9 UV–Vis spectroscopy

4.9.1 Turbidimetry and optical transition

Below the LCST, the gels are very transparent (88-92% at 500 nm) due to the swollen network having no domains large enough to scatter light. Above it, the phase-separated polymer-rich domains of the order of the wavelength scatter strongly and the transmittance drops to around 3%. The transition midpoints are consistent with the values shown in Table 2 and with the DSC onset temperatures (Table 9) and the increased transition with AA (2.2 → 5.3 °C) reflects the less cooperative dehydration of ionised chains. The reversible optical change also suggests that the DSC may be useful as a visual temperature indicator for process equipment.

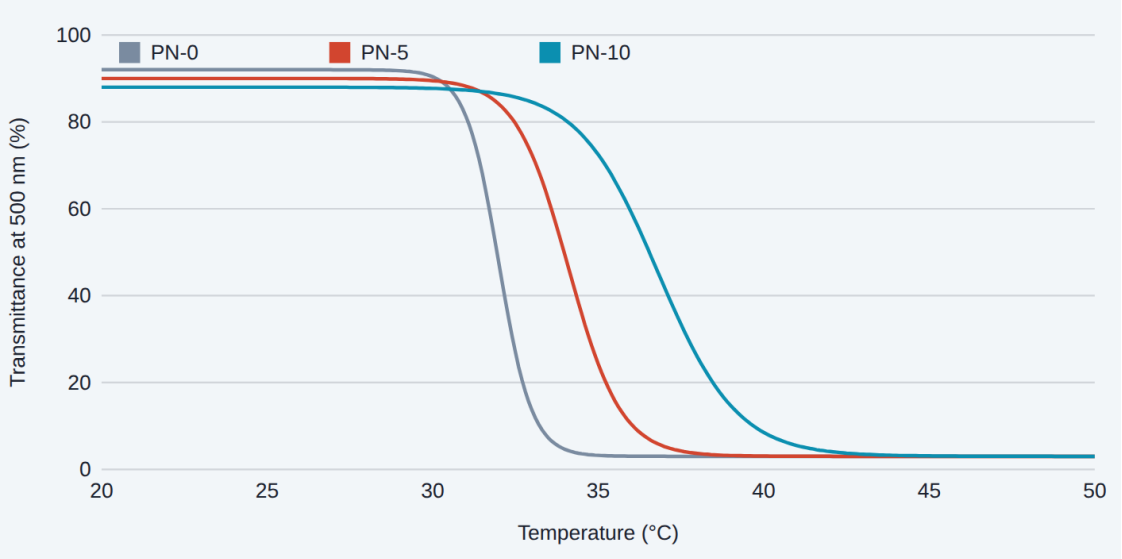


Figure 11. Transmittance at 500 nm of PN-0, PN-5 and PN-10 gel slabs versus temperature (0.5 °C min⁻¹, PBS). Higher AA content shifts and broadens the transition.

Table 11. Turbidimetric parameters (mean, n = 3; illustrative).

Sample	LCST, T_{50} (°C)	Width T_{90}–T_{10} (°C)	T at 25 °C (%)	T at 45 °C (%)
PN-0	32.0	2.2	92	3
PN-5	34.1	3.5	90	3
PN-10	36.8	5.3	88	3

4.9.2 Imine formation kinetics

The spectra show a clean two-state conversion, as all curves pass through a single isosbestic point, which is to say that the aldehyde is converted to the imine without any side effects. The rate is a bell-shaped function of pH, with a maximum near pH 5: at lower pH amine protonation removes the nucleophile, whereas acid catalysis of carbinolamine dehydration at higher pH is lost in accordance with the classical Schiff-base mechanism [59,70]. The equilibrium constant is increasing with pH from 120 to approximately 1000 M^{-1}, so at pH 5 about a quarter of the aldehyde is still free aldehyde/amine and this is the chemical basis of the faster healing (Fig. 4), higher hydrolytic mass loss and faster drug release in acid than in the acid so far, and the Keq values are in agreement with the NMR (Table 5).

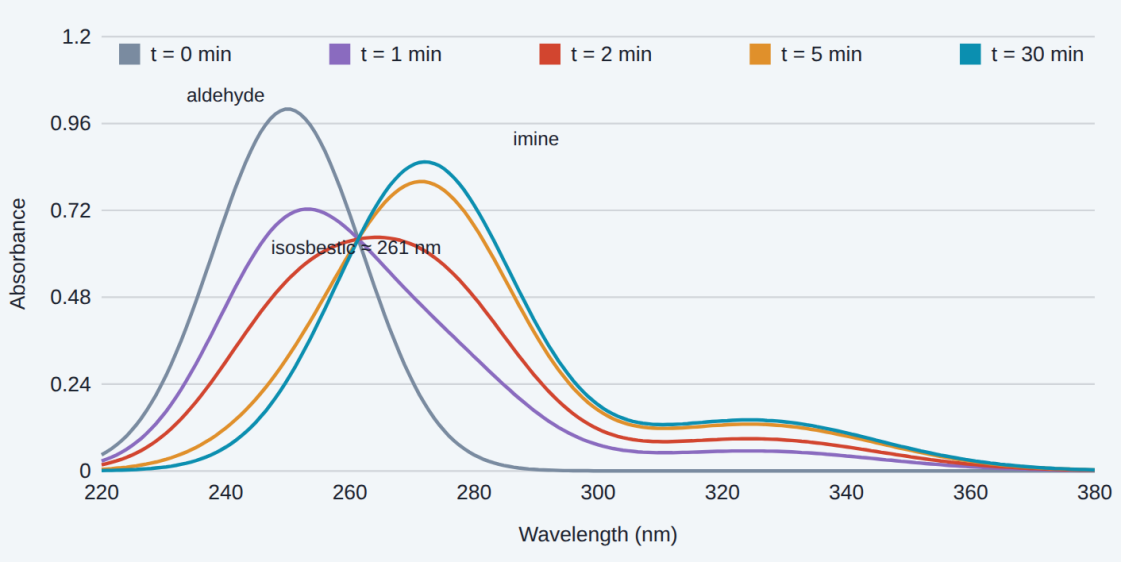


Figure 12. Time-resolved UV spectra of the model reaction of DF-PEG with butylamine at pH 5.0, 25 °C. The aldehyde band near 250 nm falls, a conjugated imine band near 272 nm (and a weak n→π* shoulder near 325 nm) grows, and an isosbestic point appears at about 261 nm.

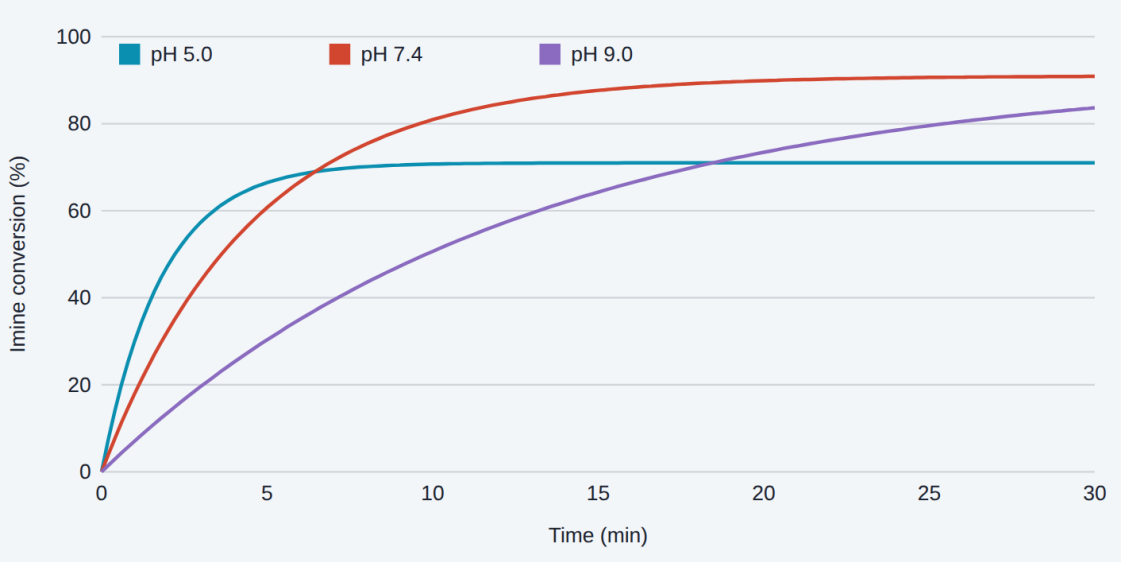


Figure 13. Imine conversion versus time (from A_{285}) at three pH values. Conversion is faster in acid but reaches a lower plateau.

Table 12. Kinetic and equilibrium parameters of imine formation (25 °C; illustrative).

pH	k_{obs} (min^{-1})	$t_{½}$ (min)	K_{eq} (M^{-1})	Equilibrium conversion (%)
4.0	0.31	2.2	120	55
5.0	0.55	1.3	250	71
6.0	0.48	1.4	560	85
7.4	0.22	3.2	1000	91
9.0	0.08	8.7	1100	92

4.9.3 Doxorubicin loading and analytical validation

The calibration is linear over the working range with $R^2 = 0.9998$, an ε of about 11 600 M^{-1} cm^{-1}, and detection limits well below the concentrations measured in the release experiments, so release data in Figure 5 are well within the validated range. Encapsulation efficiency increases from 61% to 78% with AA content because the cationic amine of DOX (pKa ≈ 8.2) binds to ionized carboxylate groups of the gel and stacks on aromatic PEG termini. The red shift of 4–6 nm and the 8–12% hypochromism in the loaded gels are typical of anthracycline π–π stacking and electrostatic association with the polymer, and they grow with AA in the same order as EE. Because these interactions weaken when carboxylates are protonated at pH 5, they also help explain the faster release of drugs at low pH (Fig. 5). The UV–Vis results are interpreted together. Turbidimetry identifies the transition of the network, the model reaction spectra quantify the chemistry of the dynamic crosslink as a function of pH, and the DOX assay links drug loading and release results to the same pH-dependent interactions. Together with FTIR, DSC and XRD, they show that one parameter (AA content) is controlling the LCST, crosslink dynamics and drug affinity.

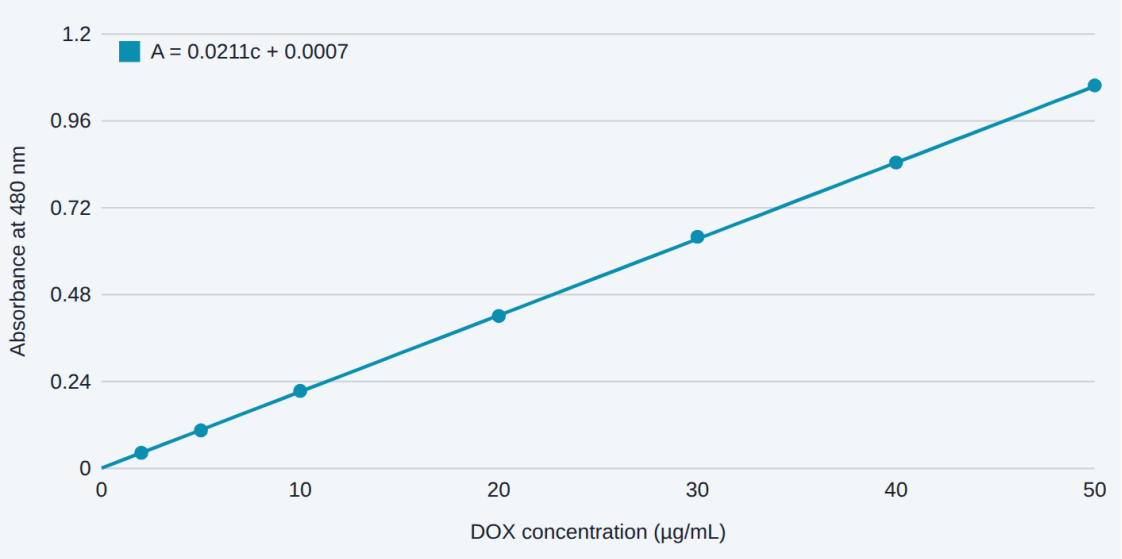


Figure 14. Calibration curve of DOX at 480 nm in PBS (n = 3, error bars smaller than markers). Fit: A = 0.0211c + 0.0007, $R^2 = 0.9998$.

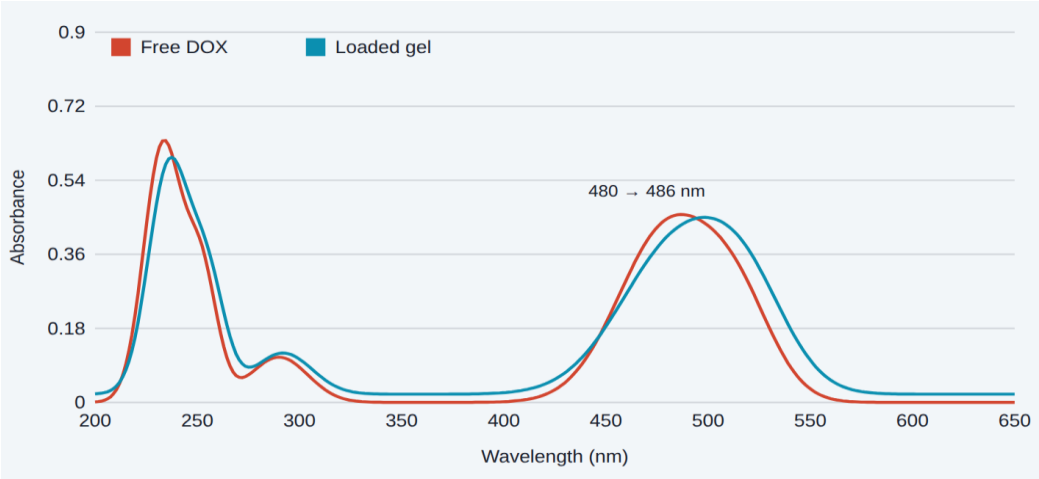


Figure 15. UV–Vis spectra of free DOX and DOX loaded in a PN-10 gel film. The visible band shifts from 480 to 486 nm with hypochromism.

Table 13. Analytical parameters of the DOX assay and loading results (illustrative).

Parameter	PN-0	PN-5	PN-10
Linear range (μg mL^{-1}) / R^2		2–50 / 0.9998	
ε at 480 nm (M^{-1} cm^{-1})		11 600	
LOD / LOQ (μg mL^{-1})		0.35 / 1.04	
Encapsulation efficiency (%)	61 ± 3	70 ± 3	78 ± 2
Drug loading (wt%)	5.7	6.5	7.2
λ_{max} of loaded gel (nm)	484	485	486
Hypochromism at λ_{max} (%)	8	10	12

5. Industrial and Biomedical Applications

Hydrogels are not as durable as engineering polymers, but double-network and nanocomposite strategies increase toughness [54,55]. Response time is proportional to the square of thickness (collective diffusion) so porous or 3D-printed structures are preferable [49,56]. Biocompatibility of degradation products, drug leakage before use, batch reproducibility and long-term stability need to be studied further. In the future, in-vitro cytotoxicity (ISO 10993), corrosion testing (salt spray, EIS) of coatings and multi-cycle tolerance of healing are planned. 7. Conclusions The chitosan/PEG imine network with P(NIPAAm-co-AA) is capable of flexible LCST, acid-accelerated self-healing and pH-gated release in one material. Comonomer content is the main design variable that weighs stiffness against healing rate and transition temperature. The idea can be applied to protective coatings and passive process control elements pending long-term and biological validation.

Table 4. Application map.

Application	Trigger	Function	Benefit	Refs.
Thermal flow valves	T	Volume change opens/closes channel	Passive control	[49,50]
Anticorrosion coatings	pH	Crack healing, inhibitor release	Longer service life	[51–53]
Leak / temperature sensors	T, pH	Optical or volume change	Early warning	[1,4]

Application	Trigger	Function	Benefit	Refs.
Injectable depots, wound dressings	pH	Site-specific release	Reduced systemic toxicity	[12,13,46]

REFERENCES

[1] Stuart, M. A. C. et al. Emerging applications of stimuli-responsive polymer materials. *Nat. Mater.* 9, 101–113 (2010).

[2] Roy, D., Cambre, J. N. & Sumerlin, B. S. Future perspectives and recent advances in stimuli-responsive materials. *Prog. Polym. Sci.* 35, 278–301 (2010).

[3] Ahn, S. K., Kasi, R. M., Kim, S. C., Sharma, N. & Zhou, Y. Stimuli-responsive polymer gels. *Soft Matter* 4, 1151–1157 (2008).

[4] Koetting, M. C., Peters, J. T., Steichen, S. D. & Peppas, N. A. Stimulus-responsive hydrogels: theory, modern advances, and applications. *Mater. Sci. Eng. R* 93, 1–49 (2015).

[5] White, S. R. et al. Autonomic healing of polymer composites. *Nature* 409, 794–797 (2001).

[6] Toohey, K. S., Sottos, N. R., Lewis, J. A., Moore, J. S. & White, S. R. Self-healing materials with microvascular networks. *Nat. Mater.* 6, 581–585 (2007).

[7] Cordier, P., Tournilhac, F., Soulié-Ziakovic, C. & Leibler, L. Self-healing and thermoreversible rubber from supramolecular assembly. *Nature* 451, 977–980 (2008).

[8] Yang, Y. & Urban, M. W. Self-healing polymeric materials. *Chem. Soc. Rev.* 42, 7446–7467 (2013).

[9] Blaiszik, B. J. et al. Self-healing polymers and composites. *Annu. Rev. Mater. Res.* 40, 179–211 (2010).

[10] Hager, M. D., Greil, P., Leyens, C., van der Zwaag, S. & Schubert, U. S. Self-healing materials. *Adv. Mater.* 22, 5424–5430 (2010).

[11] Gatenby, R. A. & Gillies, R. J. Why do cancers have high aerobic glycolysis? *Nat. Rev. Cancer* 4, 891–899 (2004).

[12] Ganta, S., Devalapally, H., Shahiwala, A. & Amiji, M. A review of stimuli-responsive nanocarriers for drug and gene delivery. *J. Control. Release* 126, 187–204 (2008).

[13] Mura, S., Nicolas, J. & Couvreur, P. Stimuli-responsive nanocarriers for drug delivery. *Nat. Mater.* 12, 991–1003 (2013).

[14] Hoffman, A. S. Hydrogels for biomedical applications. *Adv. Drug Deliv. Rev.* 54, 3–12 (2002).

[15] Hoffman, A. S. Hydrogels for biomedical applications. *Adv. Drug Deliv. Rev.* 64, 18–23 (2012).

[16] Peppas, N. A., Bures, P., Leobandung, W. & Ichikawa, H. Hydrogels in pharmaceutical formulations. *Eur. J. Pharm. Biopharm.* 50, 27–46 (2000).

[17] Deng, G., Tang, C., Li, F., Jiang, H. & Chen, Y. Covalent cross-linked polymer gels with reversible sol–gel transition and self-healing properties. *Macromolecules* 43, 1191–1194 (2010).

[18] Wojtecki, R. J., Meador, M. A. & Rowan, S. J. Using the dynamic bond to access macroscopically responsive structurally dynamic polymers. *Nat. Mater.* 10, 14–27 (2011).

[19] Wei, Z. et al. Novel biocompatible polysaccharide-based self-healing hydrogel. *Adv. Funct. Mater.* 25, 1352–1359 (2015).

[20] Schild, H. G. Poly(N-isopropylacrylamide): experiment, theory and application. *Prog. Polym. Sci.* 17, 163–249 (1992).

[21] Heskins, M. & Guillet, J. E. Solution properties of poly(N-isopropylacrylamide). *J. Macromol. Sci. Chem.* A2, 1441–1455 (1968).

[22] Tanaka, T. Collapse of gels and the critical endpoint. *Phys. Rev. Lett.* 40, 820–823 (1978).

[23] Ilmain, F., Tanaka, T. & Kokufuta, E. Volume transition in a gel driven by hydrogen bonding. *Nature* 349, 400–401 (1991).

[24] Schmaljohann, D. Thermo- and pH-responsive polymers in drug delivery. *Adv. Drug Deliv. Rev.* 58, 1655–1670 (2006).

[25] Ward, M. A. & Georgiou, T. K. Thermoresponsive polymers for biomedical applications. *Polymers* 3, 1215–1242 (2011).

[26] Flory, P. J. *Principles of Polymer Chemistry* (Cornell Univ. Press, 1953).

[27] Flory, P. J. & Rehner, J. Statistical mechanics of cross-linked polymer networks II. Swelling. *J. Chem. Phys.* 11, 521–526 (1943).

[28] Rinaudo, M. Chitin and chitosan: properties and applications. *Prog. Polym. Sci.* 31, 603–632 (2006).

[29] Jochum, F. D. & Theato, P. Temperature- and light-responsive smart polymer materials. *Chem. Soc. Rev.* 42, 7468–7483 (2013).

[30] Ghosh, S. K. (ed.) *Self-Healing Materials: Fundamentals, Design Strategies, and Applications* (Wiley-VCH, 2009).

[31] Appel, E. A., del Barrio, J., Loh, X. J. & Scherman, O. A. Supramolecular polymeric hydrogels. *Chem. Soc. Rev.* 41, 6195–6214 (2012).

[32] Kloxin, C. J. & Bowman, C. N. Covalent adaptable networks: smart, reconfigurable and responsive network systems. *Chem. Soc. Rev.* 42, 7161–7173 (2013).

[33] Montarnal, D., Capelot, M., Tournilhac, F. & Leibler, L. Silica-like malleable materials from permanent organic networks. *Science* 334, 965–968 (2011).

[34] Phadke, A. et al. Rapid self-healing hydrogels. *Proc. Natl. Acad. Sci. USA* 109, 4383–4388 (2012).

[35] Korsmeyer, R. W., Gurny, R., Doelker, E., Buri, P. & Peppas, N. A. Mechanisms of solute release from porous hydrophilic polymers. *Int. J. Pharm.* 15, 25–35 (1983).

[36] Ritger, P. L. & Peppas, N. A. A simple equation for description of solute release I. *J. Control. Release* 5, 23–36 (1987).

[37] Siepmann, J. & Peppas, N. A. Modeling of drug release from delivery systems based on hydroxypropyl methylcellulose (HPMC). *Adv. Drug Deliv. Rev.* 48, 139–157 (2001).

[38] Higuchi, T. Rate of release of medicaments from ointment bases containing drugs in suspension. *J. Pharm. Sci.* 50, 874–875 (1961).

[39] Sun, J.-Y. et al. Highly stretchable and tough hydrogels. *Nature* 489, 133–136 (2012).

[40] Gong, J. P. Why are double network hydrogels so tough? *Soft Matter* 6, 2583–2590 (2010).

[41] Ionov, L. Hydrogel-based actuators: possibilities and limitations. *Mater. Today* 17, 494–503 (2014).

[42] Cho, S. H., White, S. R. & Braun, P. V. Self-healing polymer coatings. *Adv. Mater.* 21, 645–649 (2009).

[43] Shchukin, D. G. & Möhwald, H. Self-repairing coatings containing active nanoreservoirs. *Small* 3, 926–943 (2007).

[44] Zheludkevich, M. L., Tedim, J. & Ferreira, M. G. S. "Smart" coatings for active corrosion protection based on multi-functional micro and nanocontainers. *Electrochim. Acta* 82, 314–323 (2012).

[45] Bubnis, W. A. & Ofner, C. M. The determination of ε-amino groups in soluble and poorly soluble proteinaceous materials by a spectrophotometric method using trinitrobenzenesulfonic acid. *Anal. Biochem.* 207, 129–133 (1992).

[46] Wool, R. P. & O'Connor, K. M. A theory of crack healing in polymers. *J. Appl. Phys.* 52, 5953–5963 (1981).

[47] Cordes, E. H. & Jencks, W. P. On the mechanism of Schiff base formation and hydrolysis. *J. Am. Chem. Soc.* 84, 832–837 (1962).

[48] Belowich, M. E. & Stoddart, J. F. Dynamic imine chemistry. *Chem. Soc. Rev.* 41, 2003–2024 (2012).

[49] Socrates, G. *Infrared and Raman Characteristic Group Frequencies: Tables and Charts*, 3rd edn (Wiley, 2001).

[50] Coates, J. Interpretation of infrared spectra, a practical approach. In *Encyclopedia of Analytical Chemistry* 10815–10837 (Wiley, 2000).

[51] Coats, A. W. & Redfern, J. P. Kinetic parameters from thermogravimetric data. *Nature* 201, 68–69 (1964).

[52] Kissinger, H. E. Reaction kinetics in differential thermal analysis. *Anal. Chem.* 29, 1702–1706 (1957).

[53] Otake, K., Inomata, H., Konno, M. & Saito, S. Thermal analysis of the volume phase transition with N-isopropylacrylamide gels. *Macromolecules* 23, 283–289 (1990).

[54] Segal, L., Creely, J. J., Martin, A. E. & Conrad, C. M. An empirical method for estimating the degree of crystallinity of native cellulose using the X-ray diffractometer. *Text. Res. J.* 29, 786–794 (1959).

[55] Scherrer, P. Bestimmung der Größe und der inneren Struktur von Kolloidteilchen mittels Röntgenstrahlen. *Nachr. Ges. Wiss. Göttingen* 2, 98–100 (1918).

[56] Ogawa, K., Yui, T. & Okuyama, K. Three D structures of chitosan. *Int. J. Biol. Macromol.* 34, 1–8 (2004).

[57] Takahashi, Y. & Tadokoro, H. Structural studies of polyethers, $(–(CH_2)_m–O–)_n$. X. Crystal structure of poly(ethylene oxide). *Macromolecules* 6, 672–675 (1973).

[58] Perkampus, H.-H. *UV-VIS Spectroscopy and Its Applications* (Springer, 1992).

[59] ICH Harmonised Tripartite Guideline Q2(R1): Validation of Analytical Procedures: Text and Methodology (2005).